WILEY

RESEARCH ARTICLE

On the sensitivity of the diffusion MRI signal to brain activity in response to a motor cortex paradigm

Alberto De Luca[1] | Lara Schlaffke[2] | Jeroen C. W. Siero[3,4] | Martijn Froeling[3] | Alexander Leemans[1]

[1]Image Sciences Institute, UMC Utrecht, Utrecht, The Netherlands

[2]Department of Neurology, BG-University Hospital Bergmannsheil, Ruhr-University Bochum, Bochum, Germany

[3]Department of Radiology, UMC Utrecht, Utrecht, The Netherlands

[4]Spinoza Centre for Neuroimaging, Amsterdam, The Netherlands

Correspondence
Alberto De Luca, Image Sciences Institute, UMC Utrecht, Heidelberglaan 100, 3584CX Utrecht, The Netherlands.
Email: alberto@isi.uu.nl

Abstract

Diffusion functional magnetic resonance imaging (dfMRI) is a promising technique to map functional activations by acquiring diffusion-weighed spin-echo images. In previous studies, dfMRI showed higher spatial accuracy at activation mapping compared to classic functional MRI approaches. However, it remains unclear whether dfMRI measures result from changes in the intracellular/extracellular environment, perfusion, and/or T_2 values. We designed an acquisition/quantification scheme to disentangle such effects in the motor cortex during a finger-tapping paradigm. dfMRI was acquired at specific diffusion weightings to selectively suppress perfusion and free-water diffusion, then time series of the apparent diffusion coefficient (ADC-fMRI) and of intravoxel incoherent motion (IVIM) effects were derived. ADC-fMRI provided ADC estimates sensitive to changes in perfusion and free-water volume, but not to T_2/T_2^* values. With IVIM modeling, we isolated the perfusion contribution to ADC, while suppressing T_2 effects. Compared to conventional gradient-echo blood oxygenation level-dependent fMRI, activation maps obtained with dfMRI and ADC-fMRI had smaller clusters, and the spatial overlap between the three techniques was below 50%. Increases of perfusion fractions were observed during task in both dfMRI and ADC-fMRI activations. Perfusion effects were more prominent with ADC-fMRI than with dfMRI but were significant in less than 25% of activation regions. IVIM modeling suggests that the sensitivity to task of dfMRI derives from a decrease of intracellular/extracellular diffusion and an increase of the pseudo-diffusion signal fraction, leading to different, more confined spatial activation patterns compared to classic functional MRI.

KEYWORDS
activation mapping, BOLD, diffusion MRI, free water, functional MRI, IVIM

1 | INTRODUCTION

Diffusion magnetic resonance imaging (dMRI) is a noninvasive technique sensitive to the in vivo displacement of water molecules. Despite the dynamic nature of the signal, dMRI is mostly regarded as

a structural technique providing static and reproducible snapshots of the imaged tissue (Acheson et al., 2017; Grech-Sollars et al., 2015). The dMRI signal carries information about different components of tissue microstructure. At strong diffusion weightings, the signal is mainly informative of the intracellular and extracellular environments (Winston, 2012), whereas at low diffusion weightings, it is sensitive to intravoxel incoherent motion (IVIM) phenomena, including perfusion (Le Bihan et al., 1988) and free-water diffusion (Pasternak, Sochen, Gur, Intrator, & Assaf, 2009; Pierpaoli & Jones, 2004). In the brain, the IVIM model has been used to quantify perfusion changes during CO_2 challenges (Federau et al., 2012), or in the presence of disease (Iima & Le Bihan, 2016) as cancer (Keil et al., 2017). The concept of IVIM and its applications suggest sensitivity of the dMRI signal acquired at low (i.e., $b \leq 200$ s/mm^2) to moderate b-values (i.e., $b \leq 500$ s/mm^2) to physiological dynamics in the vascular and free-water pools. In the late 1990s, dMRI data at moderate b-values were proven to be sensitive to brain activations by Song, Wong, Tan, and Hyde (1996) that originally showed how low diffusion weightings can be used to remove the contribution of major vessels during functional activations mapping.

At intermediate diffusion weightings (i.e., $1400 \geq b \geq 1000$ s/mm^2), the dMRI signal measured in the brain originates mainly from hindered (intracellular and extracellular) components, where structure and not function is assumed to be fairly constant over short time spans. In other words, if dMRI is assumed to be insensitive to function, it is also reasonable to consider that it is static, implying that the signal should not change over time beyond experimental noise. Nevertheless, an increasing number of reports are challenging the static nature of dMRI at strong diffusion weightings in the brain. Darquié, Poline, Poupon, Saint-Jalmes, and Le Bihan (2001) originally observed that visual stimuli administered during a dMRI experiment caused a small but reproducible reduction of the apparent diffusion coefficient (ADC) computed with data repeatedly acquired at both low ($b = 200$ s/mm^2) and intermediate diffusion weightings ($b = 1400$ s/mm^2). In a later experiment, which included more diffusion weightings (Le Bihan, Urayama, Aso, Hanakawa, & Fukuyama, 2006), the authors proposed a biexponential formulation based on a slow and fast pool model, and observed a 1.7% expansion of the slower diffusion pool during visual stimuli. In the conclusions of their work, cell swelling after neuronal firing was proposed as an explanation of the findings. Other reports have independently confirmed the potential of diffusion functional MRI (dfMRI) in terms of improved spatial localization of brain activations as compared to standard gradient-echo blood oxygenation level-dependent fMRI (GE-BOLD) (Song, Woldorff, Gangstead, Mangun, & McCarthy, 2002), and showed that it well represents underlying neuronal activity in rats (Nunes, Ianus, & Shemesh, 2019). Furthermore, the response function (RF) of the dfMRI signal, a mathematical description that relates the stimulation paradigm to signal changes, has been shown to have a shorter time to peak compared to GE-BOLD (Aso et al., 2009), which can be considered to be supporting the neuronal firing theory.

Despite these observations, most of the mechanisms of dfMRI, as well as its feasibility and usefulness, are yet to be investigated. Miller et al. (2007) challenged the neuronal firing theory, suggesting a major role of perfusion via the "T_2 shine through" effect (Provenzale, Engelter, Petrella, Smith, & MacFall, 1999) on the dfMRI signal. Furthermore, previous reports have observed both increases (Song et al., 1996; Song et al., 2002) and decreases (Darquié et al., 2001; Le Bihan et al., 2006) in water mobility during task, depending on whether they acquired data with either low (Song et al., 2002) or intermediate to strong diffusion weightings (Darquié et al., 2001; Le Bihan et al., 2006; Nicolas, Gros-Dagnac, Aubry, & Celsis, 2017; Williams, McMahon, Hocking, & Reutens, 2014). Such strong dependency of dfMRI on the applied diffusion weightings suggests that different microscopic processes might simultaneously take place during brain activation and deserves further investigation. Moreover, evidence beyond the visual cortex is limited (Aso, Urayama, Fukuyama, & Le Bihan, 2013; Song et al., 2002).

In this work, we investigated whether the dfMRI signal measured at increasing diffusion weightings, and derived time series, such as the ADC-fMRI, the IVIM derived signal fractions (f_{IVIM}-fMRI) and the IVIM corrected ADC (ADC$_{IVIM}$-fMRI), are sensitive to brain activations in response to a finger-tapping paradigm. In such case, we hypothesize that it is possible to disentangle the contributions of intracellular/extracellular diffusion, free-water diffusion, and blood perfusion to the observed signal changes, by taking advantage of the multiple diffusion weightings acquired in our dfMRI experiments.

2 | METHODS

In this study, we performed fMRI acquisitions while eliciting brain activations in the motor cortex with a finger-tapping task (Akhlaghi et al., 2012). Being well studied, straightforward to implement, and consisting of only two conditions (rest vs. task), this paradigm represented an excellent starting point for the investigation of the dfMRI signal in the motor cortex.

2.1 | Dataset

Seven subjects (24 ± 3 years, four females) underwent a 3 T MRI session. The experiment was approved by the local ethical committee, and informed written consent was obtained from all subjects. The data that support the findings of this study are available on request from the corresponding author. The data are not publicly available due to privacy or ethical restrictions.

2.2 | MRI acquisition

Data were acquired on a research dedicated Philips Ingenia CX scanner (Philips Medical System NV) with multiband (MB) imaging capabilities (Setsompop et al., 2012) and a 32-channel head coil. The acquisition protocol consisted of anatomical 3D T_1-weighted imaging, a GE-BOLD, and two dfMRI acquisitions. The main imaging parameters of each sequence are reported in Table 1. The dfMRI sequence was spin-echo (SE) EPI with monopolar Stejskal–Tanner gradients of varying amplitude. Three volumes were sampled for each diffusion weighting sampling

TABLE 1 Imaging parameters of the sequences employed in this study. No slice gap was employed for any of the sequences. All functional acquisitions were performed with echo planar imaging readout. Data at b = 300, 800, and 1200 s/mm^2 were acquired with gradients along three orthogonal directions aligned with the scanner axes

Sequence	Resolution (mm^3)	MB	SENSE	TE (ms)	TR (ms)	Slices	FOV (mm^3)	b-values (s/mm^2)	Bandwidth in PE (Hz)	Duration
T$_1$-w	$1 \times 1 \times 1$	–	2, 2.6	3.7	8	180	$256 \times 256 \times 180$	–	191.5	3 min 54 s
GE-BOLD	$2.5 \times 2.5 \times 3$	2	2	30	2000	52	$240 \times 240 \times 156$	–	34.2	6 min 40 s
dfMRI 1	$2.5 \times 2.5 \times 4$	2	2	85	8000	14	$240 \times 240 \times 56$	0, 300, 800	35.0	6 min 50 s
dfMRI 2	$2.5 \times 2.5 \times 4$	2	2	91	8000	14	$240 \times 240 \times 56$	0, 300, 1200	33.9	6 min 50 s

Abbreviations: dfMRI, diffusion fMRI; fMRI, functional magnetic resonance imaging; FOV, field of view; GE-BOLD, gradient-echo blood oxygenation level dependent; MB, multiband; PE, phase encoding; SENSE, sensitivity encoding parallel imaging acceleration; TE, echo time; TR, repetition time.

orthogonal gradients aligned with the main scanner axis, i.e. vectors [1 0 0], [0 1 0], and [0 0 1], respectively. The characteristic times of the gradients were Δ/δ = 48.7/23.7 ms for the first run, and Δ/δ = 52.8/27.6 ms for the second run. The echo time of the two dfMRI sequences was set to shortest, resulting in a 6 ms difference to accommodate the longer diffusion weightings employed in the second run. The second dfMRI run of one subject was not completed due to time constraints.

2.3 | Functional acquisitions

To elicit motor activation, we implemented a previously reported experiment design (Nicolas et al., 2017), which alternates six repetitions of rest and activation blocks with 32 s duration (384 s in total). Instructions were presented on a video device installed in the MR scanner room, and the start condition (task or rest) was pseudo-randomized across subjects (five subjects started with task blocks, whereas two with rest blocks). Three functional datasets were acquired for each subject. The first acquisition was a GE-BOLD sequence featuring 16 dynamics repeated over six task and six rest blocks, for a total of 192 volumes. The second and the third acquisitions were dfMRI sequences with four dynamics per diffusion weighting, repeated in six task and six rest blocks, for a total of 48 volumes per diffusion weighting and 48 nonweighted images (b = 0 s/mm^2), which are also referred to as SE-BOLD (Glielmi, Xu, Craddock, & Hu, 2010). The acquisition of multiple diffusion weightings resulted in less dynamics per block compared to a GE-BOLD acquisition. However, with these data, we can investigate different microstructural components, as explained in the following section.

2.4 | Separating physiological contributions with dfMRI, ADC, and IVIM

According to the traditional IVIM theory (Le Bihan et al., 1988), the diffusion MRI signal measured in vivo arises from both cellular and IVIM contributions. Recently, it has been shown that not only vascular contributions, but also water diffusing in large extracellular or perivascular spaces, commonly referred to as free water, contributes to the IVIM phenomenon (Rydhög et al., 2017). In this work, we leverage the acquisition of dfMRI data at multiple diffusion weightings to separate the signal into intracellular/extracellular and IVIM contributions, as explained in the following paragraphs.

The GE-BOLD signal is T$_2$* weighted and is sensitive to changes in blood volume, blood flow, and oxygenation. The SE dfMRI images are sensitive to changes in tissue diffusion, as well as in T$_2$ and in (blood) water compartment volumes (the vasculature, intracellular and extracellular water, and free water), according to the multicompartment signal model we will use here. The signal S measured at time t_j, echo time T_E, and diffusion weighting b, can be expressed as:

$$S(t_j) = S_0 \sum_i f_i e^{-\frac{T_E}{T_{2,i}(t_j)}} e^{-b D_i(t_j)} \tag{1}$$

In Equation (1), S_0 is the nonweighted signal, whereas f_i is the signal fraction, $T_{2,i}$ is the T$_2$ value, and D_i the is diffusion coefficient of the ith component. Adjusting the diffusion weighting in the dfMRI experiment allows one to selectively suppress specific contributions. Data acquired at b = 0 s/mm^2 (SE-BOLD) are sensitive to all tissue components, whereas data at b = 300 s/mm^2 are considered largely free of contributions from large vessels and part of the capillary network (e.g., signal change <5% for spins diffusing faster than 10×10^{-3} mm^2/s) (Chandarana, Lee, Hecht, Taouli, & Sigmund, 2011; Federau et al., 2015; Finkenstaedt et al., 2017). At stronger diffusion weightings, as b = 800 s/mm^2 and b = 1200 s/mm^2, the signal is considered to be insensitive to most vascular contributions (e.g., signal change <5% for spins diffusing faster than 3.7×10^{-3} and 2.5×10^{-3} mm^2/s, respectively). Data acquired at b = 1200 s /mm^2 are also negligibly sensitive to contributions from free-water diffusion, as its signal is attenuated by over 96% at that diffusion weighting.

If the tissue composition is monocompartmental, that is, i = 1 in the above equation, all dfMRI data are sensitive to T$_2$ changes independently from the applied diffusion weighting. However, if T$_2$ changes take place only in specific components, for instance, only in the vascular network, dfMRI data acquired at $b \geq 300$ s/mm^2 should be insensitive to such effects. In addition to the T$_2$ sensitivity, the EPI readout of the used dfMRI sequence is to some extent sensitive to T$_2$* changes—and hence to the BOLD contrast—but to a much lesser extent than conventional T$_2$* weighted GE-BOLD (Goense & Logothetis, 2006).

If the acquired dfMRI data contain at least two diffusion weightings, it is possible to compute the ADC over time (ADC-fMRI). ADC-fMRI is regarded as insensitive to T$_2$ and T$_2$* effects, as such dependencies cancel out in the ADC equation. However, this is only true for a monocomponent tissue formulation (i = 1). If multiple

components coexist in one voxel, ADC-fMRI becomes sensitive to factors affecting the $b = 0$ s/mm^2 image, such as perfusion and free water volume changes, among others.

If the dfMRI experiment features three or more diffusion weightings with appropriate values, it is possible to subdivide the signal contributions into an intracellular/extracellular component and an IVIM component, applying the IVIM model in a biexponential formulation ($i = 2$):

$$\frac{S}{S_0} = f_{IVIM}e^{-bD^*} + (1 - f_{IVIM})e^{-bADC_{IVIM}} \qquad (2)$$

In Equation (2), f_{IVIM} represents the signal fraction of a component including both vascular (pseudo-diffusion) and free-water contributions with diffusion coefficient D*, whereas ADC_{IVIM} is the diffusion coefficient of both intracellular and extracellular diffusion corrected for IVIM contamination. Equation (2) assumes that all nontissue diffusion terms will contribute only to the first term, but a more thorough decomposition of the signal should also account for the presence of free-water (including blood water) explicitly (Rydhög et al., 2017). This is, however, unfeasible in this study as such decomposition would require four or more diffusion weightings. Under the above mentioned assumptions, the temporal series of f_{IVIM} (in the following, referred to as f_{IVIM}-fMRI) reflects the signal fraction changes related to free-water/perfusion and is theoretically less sensitive to T_2 and T_2^* contamination than ADC-fMRI, whereas the temporal series of ADC_{IVIM} (in the following, referred to as ADC_{IVIM}-fMRI) summarizes intracellular/extracellular diffusion changes.

2.5 | Data preprocessing

GE-BOLD data of each subject were corrected for subject motion using the FSL (Jenkinson, Beckmann, Behrens, Woolrich, & Smith, 2012) tool MCFLIRT (Jenkinson, Bannister, Brady, & Smith, 2002), realigning all volumes to the first volume. Individual GE-BOLD data were used as the space of reference for all functional analyses.

The processing pipeline applied to dfMRI data is elucidated in Figure 1. The two dfMRI series were concatenated, corrected for subject motion and eddy currents using ExploreDTI (Leemans, Jeurissen, Sijbers, & Jones, 2009), aligning all dfMRI volumes to the first $b = 0$ s/mm^2 image. The first nonweighted image was registered to the individual fMRI space using a nonlinear b-spline transformation restricted to the phase-encoding direction (Klein, Staring, Murphy, Viergever, & Pluim, 2010), then all the data were transformed with a single interpolation step. Brain extraction was performed on the dfMRI data with FSL BET (Smith, 2002). The dMRI data corresponding to each diffusion weighting (b-value) were geometrically averaged. To determine the signal to noise ratio (SNR) of the data, a homogeneous region was manually delineated on an axial slice of each subject. The SNR was determined as ratio between spatial average and SD and corrected for the Rician nature of the noise (Gudbjartsson & Patz, 1995). The temporal SNR (tSNR) of all dataset was determined within the same ROI as temporal average divided by temporal SD.
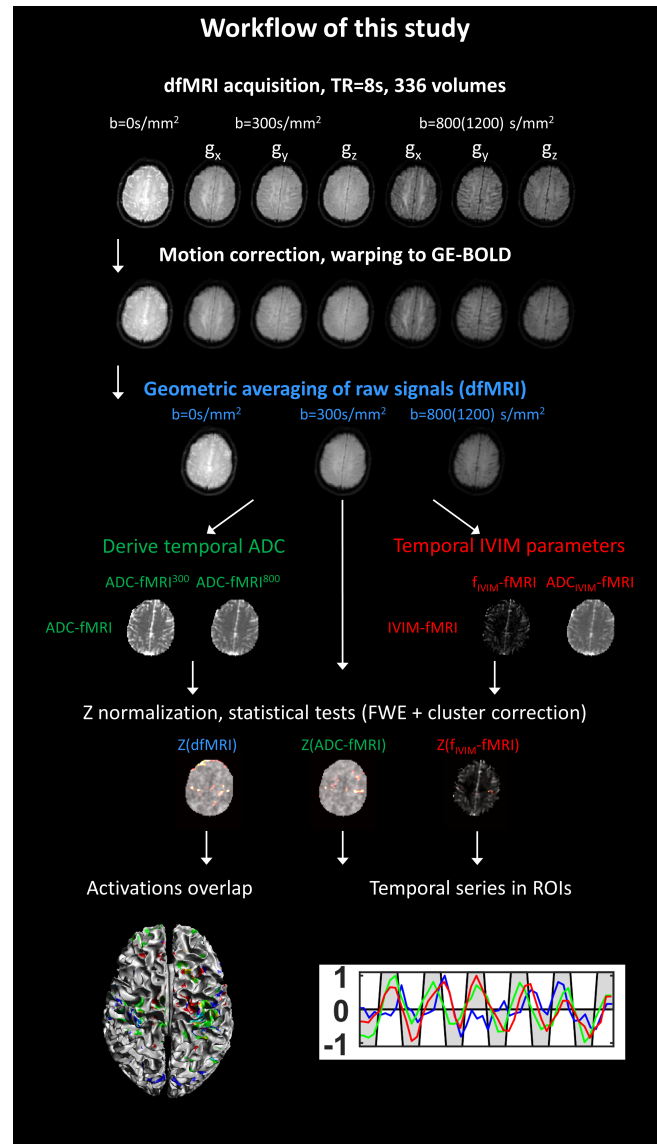

FIGURE 1 Workflow of this study. dfMRI data are first processed to attenuate motion and eddy currents-related artifacts, then warped to the individual GE-BOLD space, which is used as standard space for all analysis. Data are geometrically averaged per diffusion weighting and used (a) directly for activation mapping or (b) to derive ADC-fMRI and IVIM-fMRI. After activations are individually mapped, temporal series of the signals in the activation ROIs are computed. ADC-fMRI, apparent diffusion coefficient-functional magnetic resonance imaging; dfMRI, diffusion fMRI; $g_{x,y,z}$, diffusion gradient along the x, y, or z axis; FWE, familywise error; GE-BOLD, gradient-echo blood oxygenation level dependent; IVIM, intravoxel incoherent motion; TTP$_{1,2}$, time-to-peak of the two gamma functions [Color figure can be viewed at wileyonlinelibrary.com]

The FreeSurfer reconstruction pipeline (Dale, Fischl, & Sereno, 1999) was applied to T_1-weighted data to derive the grey matter (GM)/white matter (WM) interface used for the graphical representations. Further, the FSL pipeline "fsl_anat" (Jenkinson et al., 2012; Smith, 2002; Zhang, Brady, & Smith, 2001) was applied to each T1 image to derive segmentation of GM and WM, which were registered to the fMRI space with

elastix (Klein et al., 2010) using a b-spline registration (Klein, Staring, & Pluim, 2007).

2.6 | dfMRI, ADC, and IVIM processing

We performed Z-normalization of the dfMRI data, that is, we subtracted from each time series its average value and divided it by the SD, independently for each diffusion weighting. We then concatenated the normalized data to maximize the statistical power in the subsequent analyses.

The ADC-fMRI estimates were computed by combining the data at $b = 0$ s/mm^2 with the data at $b = 300$ s/mm^2 (ADC-fMRI^{300}), $b = 800$ s/mm^2 (ADC-fMRI^{800}), and $b = 1200$ s/mm^2 (ADC-fMRI^{1200}) separately, using the classic log ratio solution of the ADC equation (MATLAB R2016b; The MathWorks Inc.). Each ADC-fMRI series was normalized independently and then concatenated.

The IVIM fit of the data was performed by using a biexponential formulation (Cho et al., 2015), and an ordinary linear least-squares segmented fit method (Sigmund et al., 2012) (MATLAB R2016b; The MathWorks Inc.). Accordingly, perfusion corrected ADC values were computed using data at two diffusion weightings, while the normalized difference between the measured and the estimated nonweighted signal represented the perfusion fractions. Values of perfusion fractions (f_{IVIM}-fMRI) and of the perfusion corrected ADC (ADC$_{IVIM}$-fMRI) over time were computed for both the first (f_{IVIM}-fMRI^{300,800}, ADC$_{IVIM}$-fMRI^{300,800}) and the second acquisition (f_{IVIM}-fMRI^{300,1200}, ADC$_{IVIM}$-fMRI^{300,1200}). The abovementioned approaches are schematically summarized in Figure 1.

The merged Z(dfMRI), Z(ADC-fMRI), and Z(f_{IVIM}-fMRI^{300,800}) time series featured 288, 192, and 48 volumes, respectively.

2.7 | Activation ROIs mapping

Task-induced activations were mapped on the GE-BOLD data using FSL FEAT with cluster correction for multiple comparisons. Voxel-wise Z-statistics were computed by convolving the paradigm design with the default hemodynamic RF (HRF), a gamma function with average delay 3 s and SD 6 s (Glover, 1999). The Z-statistics were corrected for multiple comparisons using a first level Z-threshold equal to 0.5 and a cluster p-value equal to .05, and finally thresholded at $Z \geq 2.3$ (Nicolas et al., 2017). The statistical analysis of Z(dfMRI), Z(ADC-fMRI), Z(ADC$_{IVIM}$-fMRI), and Z(f_{IVIM}-fMRI) was performed similarly to that of GE-BOLD but employing a boxcar RF instead of the default HRF. Flattened projection maps of the Z-scores of the spatial activations with GE-BOLD, dfMRI, and ADC-fMRI can be found in the Supporting Information.

2.8 | Time series in activation ROIs

Statistically significant ROIs of Z(dfMRI) and Z(ADC-fMRI) were thresholded above 70% of their peak value to determine their activation core (AC) (Nicolas et al., 2017), here defined as AC(dfMRI) and AC(ADC-fMRI), respectively. dfMRI at each diffusion weighting, ADC-

fMRI and GE-BOLD were corrected for linear trends, divided by their maximum value, spatially averaged within the AC ROIs and temporally processed with a three-points moving average filter, to mitigate high frequency noise.

Further, the Z-scores of the average GE-BOLD, dfMRI, and ADC-fMRI signals of each subject were computed and overlaid to investigate the sensitivity of the signals to task, as well as to qualitatively observe temporal aspects—for example, lags in their response. To compute the Z-scores, the signals were corrected for linear trends and divided by their SD after demeaning.

Relative percent changes of dfMRI, ADC-fMRI, and f_{IVIM}-fMRI between the task and rest conditions were derived for each subject. The signals were averaged within the ROIs and over time within the corresponding blocks, then statistical significance was assessed with Z-tests.

2.9 | Spatial overlap of activation ROIs

The spatial agreement between two spatial activation maps, referred as A and B, was quantified using the overlap metric, which is defined as:

$$\text{OVERLAP}(A, B) = \frac{|A \cap B|}{\min(|A|, |B|)} \quad (3)$$

with the operator |A| indicating the volume of A.

Comparisons were performed between GE-BOLD, dfMRI, and ADC-fMRI. Furthermore, the effect of perfusion on dfMRI and ADC-fMRI was quantified by computing their overlap with f_{IVIM}-fMRI activations. Projection maps of the Z-scores of the overlaps between GE-BOLD, dfMRI, and ADC-fMRI were computed by summing their values along the feet-head direction, to qualitatively appreciate their extents in a planar format. These maps can be found in the Supporting Information. Finally, to understand whether dfMRI and ADC-fMRI activations were specific of GM or WM processes, we computed the overlap between the segmentations derived from the T1 images and GE-BOLD, dfMRI, and ADC-fMRI activations.

3 | RESULTS

3.1 | Diffusion fMRI

The average SNR and tSNR of the acquired dataset are reported in Table 2. Both the SNR and the tSNR of dfMRI data were sufficient and comparable to GE-BOLD up to $b = 800$ s/mm^2, while ADC-fMRI provided remarkably lower values. Figure 2 shows the 3D mapping on the WM/GM interface of the activations detected in correspondence of the task > rest condition with dfMRI, GE-BOLD, and their overlap. Bilateral activation in the primary motor cortex area is observed on the dfMRI activation maps of all subjects, whereas the supplementary motor area is detected only on two out of seven subjects. The activation maps with dfMRI include some artifactual patterns and have smaller activation clusters than those with GE-BOLD. The overlap between statistically significant voxels of dfMRI and GE-BOLD is

45 ± 14%. dfMRI activations overlapped more with GM than WM, 41 ± 7% versus 31 ± 10%, respectively. Axial projections of the activation maps and of the spatial overlap are shown in Figure S1, Supporting Information.

Time series of GE-BOLD, dfMRI (for different diffusion weightings), ADC_{IVIM}-fMRI, and f_{IVIM}-fMRI averaged within AC(dfMRI) are reported in Figure 3. All diffusion weighted signals consistently show increases in correspondence of task execution followed by decreases at rest, similarly to GE-BOLD.

TABLE 2 SNR and tSNR of GE-BOLD, dfMRI, and ADC-fMRI in each separate acquisition. GE-BOLD and dfMRI had comparable SNR levels, whereas the SNR of ADC-fMRI is remarkably lower

	SNR		tSNR	
Data	Run 1	Run 2	Run 1	Run 2
GE-BOLD	30 ± 10	NA	30 ± 9	NA
dfMRI (b = 0 s/mm^2)	33 ± 9	26 ± 5	30 ± 10	28 ± 6
dfMRI (b = 300 s/mm^2)	28 ± 9	27 ± 9	29 ± 10	28 ± 7
dfMRI (b = 800 s/mm^2)	25 ± 9	NA	23 ± 8	NA
dfMRI (b = 1200 s/mm^2)	NA	18 ± 7	NA	17 ± 4
ADC-fMRI^{300}	15 ± 4	11 ± 5	14 ± 4	11 ± 3
ADC-fMRI^{800}	18 ± 4	NA	19 ± 5	NA
ADC-fMRI^{1200}	NA	11 ± 6	NA	15 ± 3

Abbreviations: ADC, apparent diffusion coefficient; dfMRI, diffusion fMRI; fMRI, functional magnetic resonance imaging; GE-BOLD, gradient-echo blood oxygenation level dependent; NA, not applicable; SNR, signal to noise ratio; tSNR, temporal SNR.

Although all signal changes are consistent with the task-rest paradigm, signals acquired at b = 800, 1200 s/mm^2 exhibit a larger number of artifacts than those at b = 300 s/mm^2. Considering the average signals within task and rest blocks, we observe significant increases of +0.51 ± 0.20% (p = 10^{-4}), +0.34 ± 0.23% (p = 10^{-3}), +0.44 ± 0.24% (p = 10^{-3}) and +0.53 ± 0.19% (p = 10^{-4}) during the task for b = 0, 300, 800, and 1200 s/mm^2, respectively. Regarding ADC-fMRI signals in AC(dfMRI), only ADC-fMRI^{300} showed significant signal increases during task compared to rest.

ADC_{IVIM}-fMRI and f_{IVIM}-fMRI are very noisy at individual levels, but on average show response to task execution, with f_{IVIM}-fMRI$^{300-800}$ showing an increase between 4 and 5%, and ADC_{IVIM}-fMRI a decrease during finger tapping. The average changes of the considered metrics from task to rest within AC(dfMRI), and their statistical significance, are reported in Table 3.

Activations detected with f_{IVIM}-fMRI appear noisier than those with dfMRI and characterized by smaller spatial extents. The overlap between activations from the two techniques is limited, with values equal to 15 ± 14%.

Figure 4 shows the Z-values of the time series of GE-BOLD and dfMRI at multiple diffusion weightings. The sensitivity of the dfMRI signal to task is similar to that of GE-BOLD, with increases and decreases reaching ±2 SDs of the signal variation. Considering the average inter-subject signals, changes in dfMRI at b = 1200 s/mm^2 slightly preceded those of SE-BOLD (b = 0 s/mm^2).
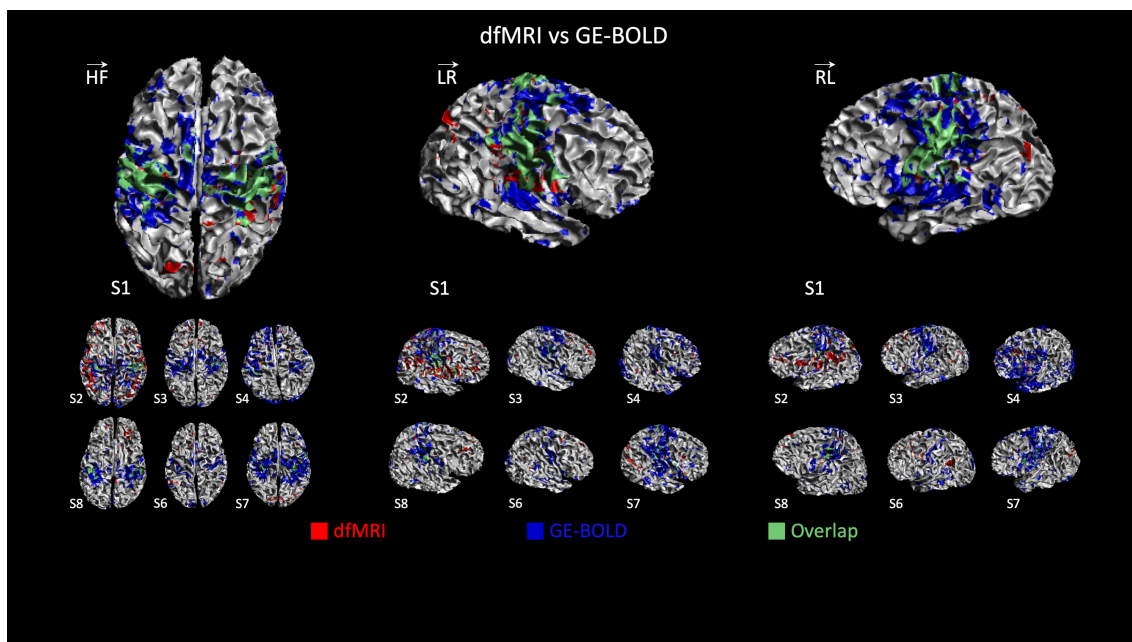

FIGURE 2 dfMRI versus GE-BOLD activation maps. Individual activation maps detected with dfMRI (red) as compared to GE-BOLD (blue), and their overlap (green) overlaid on the gray/white matter surface of each subject. Bilateral activation as response to finger tapping was observed on all subjects with both sequences. Activations with dfMRI were smaller than those with GE-BOLD. Spurious activations due to multiband reconstruction artifacts can be spotted on the dfMRI activations of some subjects. dfMRI, diffusion functional magnetic resonance imaging; GE-BOLD, gradient-echo blood oxygenation level dependent [Color figure can be viewed at wileyonlinelibrary.com]
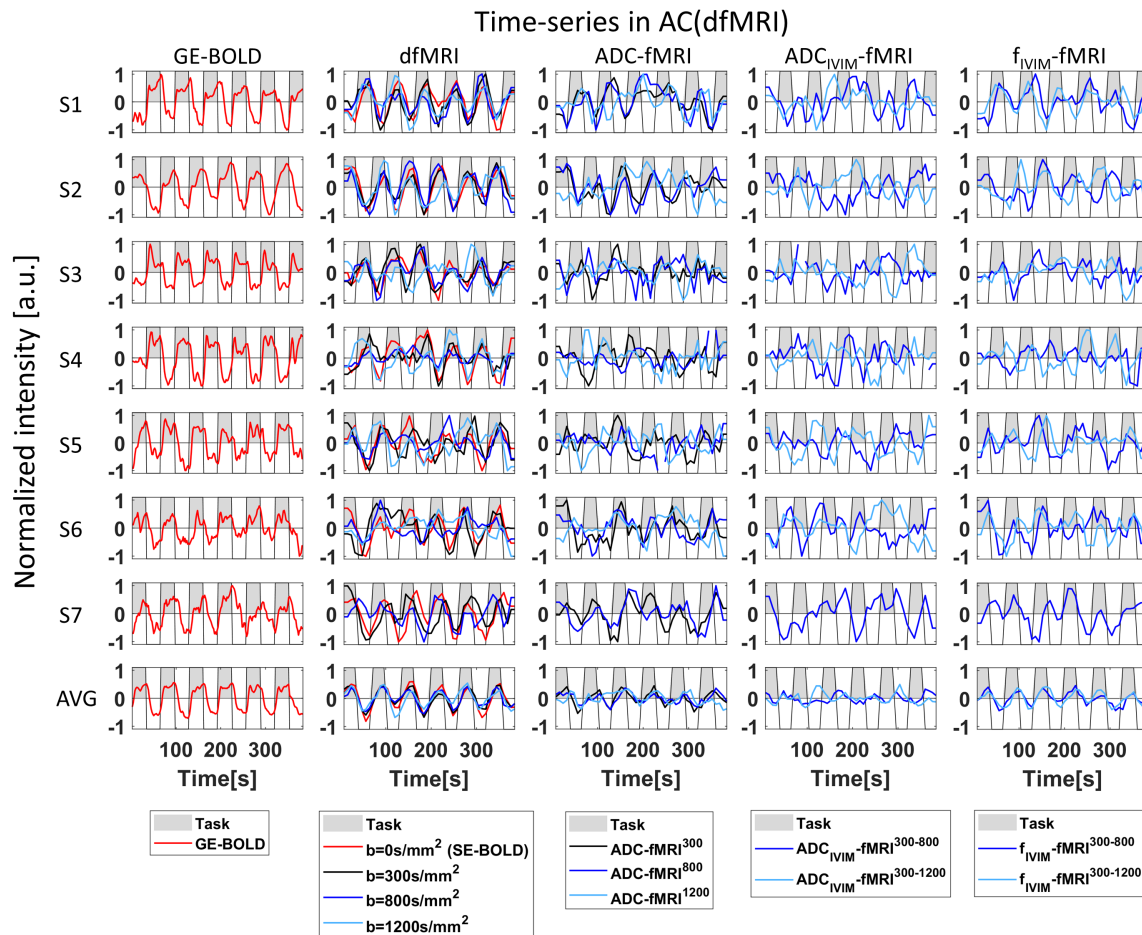
FIGURE 3 Time series in AC(dfMRI). Normalized average time series of GE-BOLD, dfMRI (for different diffusion weightings, red, black, blue, and light blue solid lines), ADC-fMRI, ADC_{IVIM}-fMRI, and f_{IVIM}-fMRI of each subject (each row), and after group averaging (last row), within the dfMRI activation ROIs. Gray blocks correspond to task execution, whereas white blocks to rest. GE-BOLD and dfMRI showed increases and decreases in correspondence of task and rest, respectively. f_{IVIM}-fMRI showed synchronization with the task execution, but to a less extent than dfMRI. The ADC_{IVIM}-fMRI signal was characterized by strong pseudo-random fluctuations, but its average variation suggested its decrease during task execution. ADC, apparent diffusion coefficient; dfMRI, diffusion functional magnetic resonance imaging; GE-BOLD, gradient-echo blood oxygenation level dependent [Color figure can be viewed at wileyonlinelibrary.com]

3.2 | ADC-functional MRI

Figure 5 shows a 3D rendering of the functional activation maps detected with ADC-fMRI, GE-BOLD, and their overlap on the GM/WM interface. Bilateral activations in the primary motor cortex are observed on all subjects with ADC-fMRI, but they have a smaller extension than those observed with dfMRI. Furthermore, activations with ADC-fMRI appear noisier compared to dfMRI. The overlap between Z(ADC-fMRI) and GE-BOLD is $33 \pm 15\%$, while the overlap between Z(ADC-fMRI) and Z(dfMRI) is the lowest, $16 \pm 10\%$. ADC-fMRI activations were equally located in GM and WM, with overlap values of $38 \pm 6\%$ and $38 \pm 4\%$, respectively. Axial projections of the activation maps of ADC-fMRI and of its spatial overlap with dfMRI and GE-BOLD are shown in Figure S1, Supporting Information.

Time series of GE-BOLD, ADC-fMRI, ADC_{IVIM}-fMRI, and f_{IVIM}-fMRI within AC(ADC-fMRI) are shown in Figure 6. The average GE-BOLD signal follows the task-rest paradigm, but to a smaller extent than in the dfMRI activations. Changes of Z(ADC-fMRI) are highly coherent with

the functional paradigm, with an increase during task followed by a decrease at rest. The first run of subject S3 does not show such behavior due to a signal discontinuity artifact approximately at the half of the acquisition. During task, significantly higher ADC values than at rest are observed, $+2.17 \pm 1.15\%$ for ADC-fMRI^{300} ($p = 10^{-3}$), $+1.14 \pm 0.57\%$ for ADC-fMRI^{800} ($p = 10^{-3}$), and $+1.18 \pm 0.76\%$ ($p = 10^{-3}$) for ADC-fMRI^{1200}. The average changes of the considered metrics from task to rest within AC(ADC-fMRI), and their statistical significance, are reported in Table 3. SE-BOLD showed significant increases in AC(ADC-fMRI) during task execution, whereas dfMRI at $b = 1200$ s/mm^2 significantly decreased in the same condition.

Within the AC(ADC-fMRI) ROIs, f_{IVIM}-fMRI$^{300-800}$ shows a strong dependence on task execution and shows an increase of on average around 7–9% during activation compared to rest. However, the overlap between ADC-fMRI activations and f_{IVIM}-fMRI$^{300-800}$ activations is relatively modest, $19 \pm 11\%$. Increases of ADC_{IVIM}-fMRI were observed during task execution within AC(ADC-fMRI), but these were significant only in one of the two runs.

TABLE 3 Values at rest of the time series of dfMRI, ADC-fMRI, ADC$_{IVIM}$-fMRI, and f_{IVIM}-fMRI in AC(dfMRI) and AC(ADC-fMRI), and their signal change during task as compared to rest. The *p*-value refers to a two-sided *t* test between the average values in the two conditions and is highlighted in bold when significant

Signal	AC(dfMRI)			AC(ADC-fMRI)		
	Average value	Signal change	*p*-Value	Average value	Signal change	*p*-Value
GE-BOLD	–	+1.02 ± 0.64	**<.01**	–	+0.72 ± 0.53	**.01**
dfMRI (b = 0 s/mm^2)	–	+0.51 ± 0.20	**<.01**	–	+0.47 ± 0.24	**<.01**
dfMRI (b = 300 s/mm^2)	–	+0.34 ± 0.23	**<.01**	–	−0.06 ± 0.18	.38
dfMRI (b = 800 s/mm^2)	–	+0.44 ± 0.24	**<.01**	–	−0.13 ± 0.31	.31
dfMRI (b = 1200 s/mm^2)	–	+0.53 ± 0.19	**<.01**	–	−0.22 ± 0.18	**.03**
ADC-fMRI^{300}	(1.11 ± 0.08) × 10^{-3} mm^2/s	+0.55 ± 0.26	**<.01**	(1.10 ± 0.11) × 10^{-3} mm^2/s	+2.17 ± 1.15	**<.01**
ADC-fMRI^{800}	(0.92 ± 0.08) × 10^{-3} mm^2/s	+0.06 ± 0.16	.37	(0.93 ± 0.09) × 10^{-3} mm^2/s	+1.14 ± 0.57	**<.01**
ADC-fMRI^{1200}	(0.85 ± 0.07) × 10^{-3} mm^2/s	+0.05 ± 0.21	.58	(0.83 ± 0.06) × 10^{-3} mm^2/s	+1.18 ± 0.76	**.01**
ADC$_{IVIM}$-fMRI$^{300-800}$	(0.83 ± 0.08) × 10^{-3} mm^2/s	−0.28 ± 0.24	**.02**	(0.84 ± 0.08) × 10^{-3} mm^2/s	+0.46 ± 0.58	.08
ADC$_{IVIM}$-fMRI$^{300-1200}$	(0.78 ± 0.06) × 10^{-3} mm^2/s	−0.26 ± 0.25	**.05**	(0.75 ± 0.08) × 10^{-3} mm^2/s	+0.56 ± 0.53	**.05**
f_{IVIM}-fMRI$^{300-800}$	0.07 ± 0.01	+3.92 ± 1.81	**<.01**	0.07 ± 0.01	+7.70 ± 3.67	**<.01**
f_{IVIM}-fMRI$^{300-1200}$	0.09 ± 0.01	+3.16 ± 2.07	**.01**	0.09 ± 0.01	+6.02 ± 2.53	**<.01**

Abbreviations: ADC, apparent diffusion coefficient; dfMRI, diffusion fMRI; fMRI, functional magnetic resonance imaging; GE-BOLD, gradient-echo blood oxygenation level dependent; NA, not applicable; SNR, signal to noise ratio; tSNR, temporal SNR.

Figure 7 shows the Z-score of the time series of GE-BOLD and ADC-fMRI computed with three different combinations of diffusion weightings. The ADC-fMRI series showed signals increases and decreases up to ±2 SDs, but their changes exhibited a consistently higher delay with task execution compared to GE-BOLD and dfMRI (Figure 4).

4 | DISCUSSION

In this work, we investigated changes in the diffusion-weighted signal measured in the brain during a motor cortex paradigm to verify whether (a) the dMRI signal acquired at different diffusion weightings is sensitive to changes evoked by the execution of a motor task; and (b) it is possible to separate the signal sources from the observed dfMRI signal changes. Our findings suggest that the dMRI signal is sensitive to task evoked changes in brain function, and that perfusion/free-water changes can explain only part of the observed signal alterations.

In all subjects, we detected clusters where the paradigm significantly explained the dfMRI signal. The activations detected with dfMRI (Figure 2) are located approximately in the same areas as observed with GE-BOLD, but their extension is markedly smaller, in line with a previous study on the visual cortex (Nicolas et al., 2017) and with previous reports comparing SE-based activation with GE-BOLD (Glielmi et al., 2010; Norris, Zysset, Mildner, & Wiggins, 2002). Furthermore, the overlap between the activations from the two techniques is limited, with values smaller than 50%, suggesting adjacent and only partially overlapping areas. The reduced extension can be explained either by the reduced temporal resolution of dfMRI as compared to GE-BOLD, or by the choice of the boxcar RF in place of a more sophisticated formulation (Aso et al., 2009). Additionally, the

signal crushing effect of the diffusion gradients on the vascular network may also reduce the activation extent and thus to lead to a more accurate spatial localization, as previously suggested (Song et al., 2002). Further, such effect is unlikely to be due to SNR, as dfMRI and GE-BOLD were characterized by similar SNR and tSNR levels, both around 30, but could be influenced by the lower number of samples collected in dfMRI as compared to GE-BOLD.

The time series reported in Figure 3 show remarkable synchronization between task execution and dfMRI signal changes at different diffusion weightings. Although the observed alterations are modest in absolute value, i.e. below 1%, they are consistent across subjects, and statistically significant ($10^{-4} < p < 10^{-2}$). Such changes are of the same order of magnitude and sign of those originally reported by Le Bihan et al. (2006), and suggest that dfMRI at weak diffusion weighting (b = 300 s/mm^2) is less sensitive to activation than both SE-BOLD (b = 0 s/mm^2) and dfMRI at intermediate to strong weighting (b = 800, 1200 s/mm^2). In our study, the average signal changes observed at b = 800 and 1200 s/mm^2 slightly anticipated changes in SE-BOLD, but to a small extent, while previous works (Aso et al., 2009; Aso et al., 2013; Le Bihan et al., 2006) reported that the time-to-peak of the dfMRI signal is considerably faster than both SE-BOLD and GE-BOLD. This might be explained by taking into consideration the repetition time employed in this work, 8 s, which is the same order of magnitude of the time offset between dfMRI and SE-BOLD reported in the above-mentioned works. An alternative interpretation is that the maximum diffusion-weighting employed in this study (b = 1200 s/mm^2), which is remarkably lower than that employed in the above-mentioned studies (b = 1600, 2400 s/mm^2), might be not sufficient to take advantage of the higher temporal resolution of dfMRI. It should also be noted that in contrast to the abovementioned studies, in this study we acquired two diffusion weightings
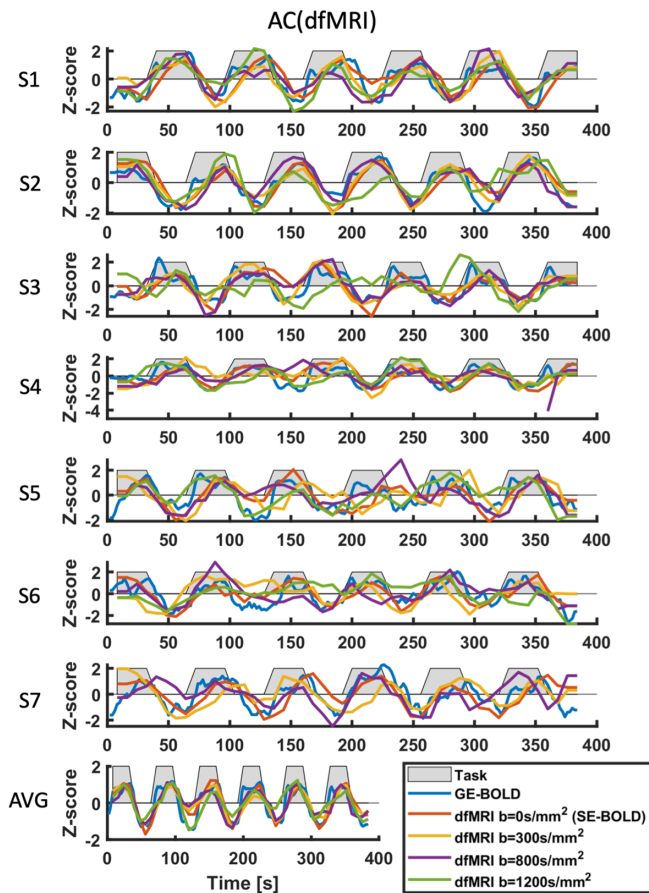
FIGURE 4 Sensitivity of GE-BOLD and dfMRI in AC(dfMRI). Z-score of the time series of GE-BOLD and dfMRI (for different diffusion weightings, red, orange, and purple solid lines) within the dfMRI activation core. The individual dfMRI signals showed signal changes up to 2 SDs in correspondence of task execution in line with GE-BOLD, irrespectively of the applied diffusion-weighting. The time series suggest that dfMRI signals at b = 1200 s/mm^2 exhibited slightly faster reactivity to task than SE-BOLD (b = 0 s/mm^2), whereas differences with GE-BOLD were minimal. dfMRI, diffusion functional magnetic resonance imaging; GE-BOLD, gradient-echo blood oxygenation level dependent; SE-BOLD, spin-echo BOLD [Color figure can be viewed at wileyonlinelibrary.com]

(in addition to b = 0 s/mm^2 volume) per run. This results in an intrinsic temporal offset of 1.5 s between different diffusion weightings, which we did not take into account. While considering such shift is not trivial, this acquisition scheme offers the advantage of acquiring multiple diffusion weightings in a reasonable time and ensures that all data experience the same task evoked condition.

A controversial point about dfMRI relates to its underlying physiological mechanisms. Some studies suggest that these mechanisms have a neuronal (or closer to) origin (Darquié et al., 2001; Le Bihan et al., 2006; Nunes et al., 2019), whereas others show a perfusion related origin (Miller et al., 2007; Rudrapatna, van der Toorn, van Meer, & Dijkhuizen, 2012). Although intermediate diffusion gradients (i.e., b = 1200 s/mm^2) are expected to completely suppress the perfusion signal, this might still affect the measured signal via the "T$_2$ shine-

through" effect (Provenzale et al., 1999). This would be especially true if the signal would originate from a single tissue component, which is not likely to be the case. To investigate this, we tailored our dfMRI acquisition design to disentangle multiple components. When using a two-component model, we observed increases of perfusion signal fractions in AC(dfMRI), between 3 and 4%. Hypothesizing invariance of the intra/extracellular environment, such perfusion changes would result in net signal alterations at b = 800 and 1200 s/mm^2 above 1%. Taking into account that ADC$_{IVIM}$-fMRI (Figure 3)—which is theoretically less influenced by perfusion/T$_2$/T$_2$* contamination—shows weak but consistent decreases in AC(dfMRI) during task execution, we suggest that in such ROI, a reduction of intracellular/extracellular diffusivity (Darquié et al., 2001; Le Bihan et al., 2006) takes place simultaneously to increases in T$_2$ and blood volume (Miller et al., 2007). Interestingly, we observed an increase of ADC-fMRI^{300} in AC(dfMRI), which seems in disagreement with previous studies. However, such result was previously observed also by Yacoub, Uludağ, Uğurbil, and Harel (2008), who reported ADC increases during activation when computing ADC from b = 1600 s/mm^2, in contrast to decreases when using data at b = 1200, 2400 s/mm^2. Indeed, when applying the IVIM decomposition (Equation (2)), we observed that a significant ADC decrease (ADC$_{IVIM}$-fMRI$^{300-800}$) and a significant perfusion fraction increase (f_{IVIM}-fMRI$^{300-800}$) take place simultaneously during activation. The increase in perfusion signal fraction can explain why previous studies employing low diffusion weightings observed ADC increases (Song et al., 1996; Song et al., 2002), whereas the reduction in intracellular/extracellular diffusivity is in line with the observation of ADC decreases (Darquié et al., 2001; Le Bihan et al., 2006) at strong diffusion weighting. These two effects are entangled and may cancel out when including data at b = 0 s/mm^2 in the ADC computation, explaining the lack of significance of changes in ADC-fMRI^{800} and ADC-fMRI^{1200} within AC(dfMRI). For this reason, we suggest deriving ADC values either with IVIM modeling or by excluding data at b = 0 s/mm^2 from the computation. This is consistent with the observation of a slightly faster responsiveness of the dfMRI signal to the neuronal stimulus at b = 1200 s/mm^2 compared to that at b = 0 s/mm^2 (Figure 4), and with our results on the poor overlap between Z(dfMRI) and $Z(f_{IVIM}$-fMRI$^{300-800})$ activations (around 15%), suggesting that perfusion is a potential contributor of the observed dfMRI changes. We further observed that dfMRI activations were mostly located in GM but also had a large component in WM, where swelling has been shown as a mechanism implicated in neuronal transmission (Fields, 2011). Changes in T$_2$* appear to have a limited influence on the dfMRI signal, provided that the detected activations were not fully included in those derived from GE-BOLD but rather exhibited an alternative spatial pattern, as suggested by the limited overlap values equal to 45 ± 14%. This is in good agreement with the study of Tsurugizawa, Ciobanu, and Le Bihan (2013), which compared GE-BOLD and dfMRI in animals under strict experimental conditions. The study showed that the activation maps detected with GE-BOLD extend well beyond those derived with dfMRI, but also that the sensitivity of the latter to activation is preserved after the removal T$_2$/T$_2$* changes by inhibition of neurovascular coupling mechanisms.
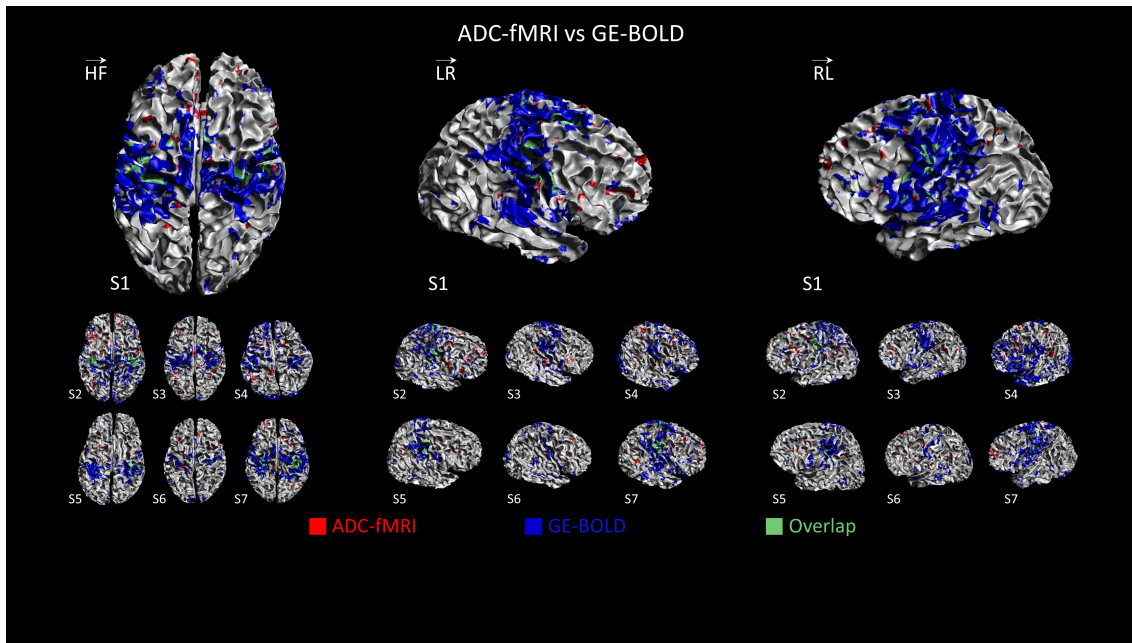
FIGURE 5 ADC-fMRI versus GE-BOLD activations maps. Individual activation maps detected with ADC-fMRI (red) as compared to GE-BOLD (blue), and their overlap (green) overlaid on the gray/white matter surface of each subject. Bilateral activation was observed on all subjects with both sequences. However, activations with ADC-fMRI were weaker than those with dfMRI, and generally did not include the supplementary motor cortex. compared to GE-BOLD, activations from Z(ADC-fMRI) had smaller extension. ADC, apparent diffusion coefficient; dfMRI, diffusion fMRI; fMRI, functional magnetic resonance imaging; GE-BOLD, gradient-echo blood oxygenation level dependent [Color figure can be viewed at wileyonlinelibrary.com]

Analysis of significantly task-activated ADC-fMRI voxels resulted in bilateral clusters partially overlapping those obtained with GE-BOLD (Figure 3), similarly to what was observed for dfMRI. Activations with ADC-fMRI are generally more confined than those from dfMRI but show less artifactual areas. Further, the supplementary motor cortex is hardly revealed, which might be partially due to the smaller sample size of ADC-fMRI series compared to dfMRI, as well as to its remarkably lower SNR values (see Table 2). Future studies performing ADC-fMRI should consider the combined penalty of reduced sample size and SNR in comparison to dfMRI, for instance, by increasing the number of collected samples. The ADC-fMRI values increase during activation between 2% (ADC-fMRI^{300}) and 1% (ADC-fMRI^{800}, ADC-fMRI^{1200}), which is in line with what is observed in the visual cortex by Nicolas et al. (2017), and in the same magnitude but opposite sign of what is originally reported by Darquié et al. (2001). Considering that f_{IVIM}-fMRI but not ADC$_{IVIM}$-fMRI (Figure 5) show significant changes during task execution in AC(ADC-fMRI), we suggest that the observed increase in ADC values is largely driven by blood volume and T_2 values changes. This result might seem counterintuitive, given the dependency of ADC from T_2 values cancels out in the ADC equation. However, such assumption holds only if the signal originates from a single water pool, that is, adhering to the classic monoexponential diffusion equation. When applying the biexponential IVIM model, our results indeed show an increase in perfusion signal fraction between 6 and 7% in the ADC-fMRI activations (Table 3), which is more than what was observed for the dfMRI activations. The activation overlap with f_{IVIM}-fMRI activations is higher with ADC-fMRI (~19%) than with dfMRI (~15%) (see also

Figure S1, Supporting Information), and f_{IVIM}-fMRI exhibits a stronger correlation with task execution in AC(ADC-fMRI) than in AC(dfMRI). ADC$_{IVIM}$-fMRI, which is theoretically less affected by perfusion effects, shows small but significant decreases during activation in AC(dfMRI), in line with previous reports on ADC during activations (Darquié et al., 2001; Le Bihan et al., 2006; Tsurugizawa et al., 2013; Yacoub et al., 2008), but also unexpected increases in AC(ADC-fMRI). Finally, changes in ADC-fMRI (Figure 7) exhibit a visible lag to task execution compared to both GE-BOLD and dfMRI (Figure 4), suggesting the latter to be closer to the early activation mechanisms. Given these observations and taking into account that ADC-fMRI activations equally cover GM and WM, we conclude that perfusion is likely to be a stronger contributor in the ADC-fMRI response compared to the dfMRI response.

Some limitations of this work must be acknowledged. Our sequence design allows to repeatedly acquire data at multiple diffusion weightings in reasonable times, allowing to simultaneously derive ADC measures and perfusion signal fractions. However, due to the inherent delay of 7 s introduced between $b = 0$ s/mm^2 volume and the last diffusion weighted volume acquired in each dynamic, the temporal resolution advantage of diffusion weighted data at strong b-value might be partially compromised if no further corrections are considered. However, the nature of our experiments does not allow to thoroughly investigate the temporal aspects of the dfMRI signal, which needs further investigation with dfMRI data acquired with shorter repetition times. The perfusion changes observed in this work are noticeably smaller than those reported in Federau et al. (2015). This might be due to simultaneous mechanisms taking place in the free water regime, which was
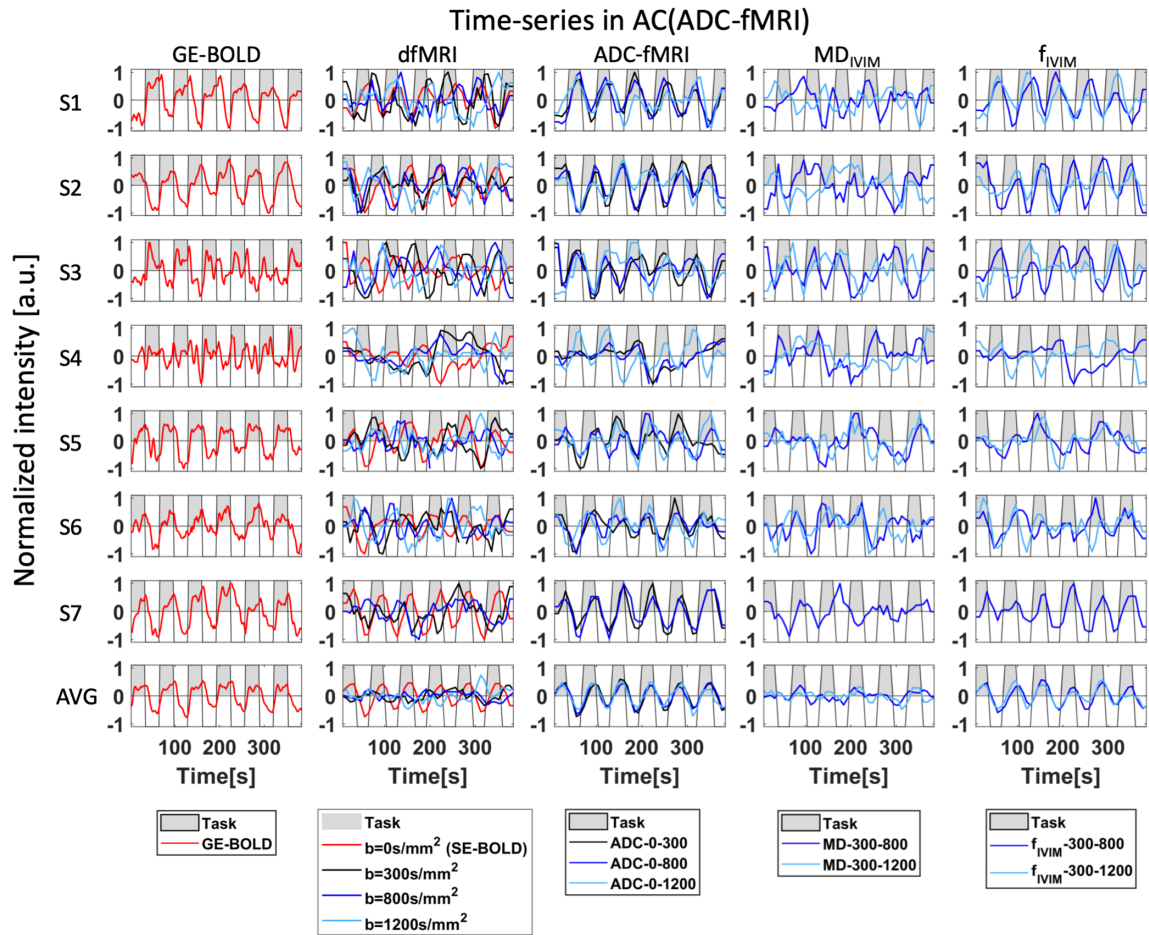
Time-series in AC(ADC-fMRI)

FIGURE 6 Time series in AC(ADC-fMRI). Normalized average time series of GE-BOLD, dfMRI (for different diffusion weightings, ADC-fMRI, ADC$_{IVIM}$-fMRI, and f_{IVIM}-fMRI of each subject (each row), and after group averaging (last row), within the ADC-fMRI activation ROIs. Gray blocks correspond to task execution, whereas white blocks to rest. GE-BOLD and ADC-fMRI showed increases and decreases in correspondence of task and rest, respectively. f_{IVIM} increases with task execution and decreases during rest were more prominent within ADC-fMRI activations than within AC(dfMRI). The average of the ADC$_{IVIM}$-fMRI signal did not exhibit clear correlations to the task. ADC, apparent diffusion coefficient; dfMRI, diffusion fMRI; fMRI, functional magnetic resonance imaging; GE-BOLD, gradient-echo blood oxygenation level dependent [Color figure can be viewed at wileyonlinelibrary.com]

suppressed with a fluid attenuated inversion recovery acquisition. Unfortunately, such acquisition is not advantageous in the dfMRI context due to the need for short repetition times. To further investigate such hypothesis, the dfMRI acquisition should be modified to accommodate a third intermediate diffusion weighting value within TR limitations. It is also worth mentioning that in Federau et al. (2015), the value of the TR was 12 times longer than the one used in this study, which affects the T1-weighting of the signal and, hence, may partially explain the observed differences. The acquisition of more diffusion weightings would also allow to employ more sophisticated IVIM fit approaches than the one here used, such as stretched exponentials (Koh, Collins, & Orton, 2011) or proper multiexponential fit (De Luca, Leemans, Bertoldo, Arrigoni, & Froeling, 2018; van Baalen et al., 2017), taking into account the diffusion coefficient of the pseudo-diffusion pool and improving fit quality. When trying to map task activations directly with ADC$_{IVIM}$-fMRI, we did not find any activation cluster, likely due to insufficient statistical power. More advanced fit strategies and a larger number of measurements are therefore needed to achieve such mapping

within clinically achievable SNR levels. A more refined modeling of the dfMRI signal could also allow, for instance, to investigate the origin behind the observed ADC$_{IVIM}$-fMRI increases in AC(ADC-fMRI). A possible explanation for such increases is the expansion of a free-water like component due, for instance, to cell swelling (Fields, 2011). Such component is not explicitly taken into account in our IVIM modeling and might therefore be erroneously assimilated to the intracellular/extracellular diffusivity component due to modeling errors.

The choice of the gradient waveform employed in a dfMRI experiment is to date not standardized and represents a further source of variability in the reported results. Previous studies have indeed employed monopolar Stejskal–Tanner gradients (Darquié et al., 2001; Nicolas et al., 2017; Yacoub et al., 2008), twice refocused SE (TRSE) acquisitions (Aso et al., 2009; Aso et al., 2013; Kohno et al., 2009; Le Bihan et al., 2006; Miller et al., 2007; Tsurugizawa et al., 2013; Williams et al., 2014), as well as less conventional waveforms (Nunes et al., 2019; Song et al., 2002). In this study, we have employed classic monopolar Stejskal–Tanner diffusion gradients, which are potentially
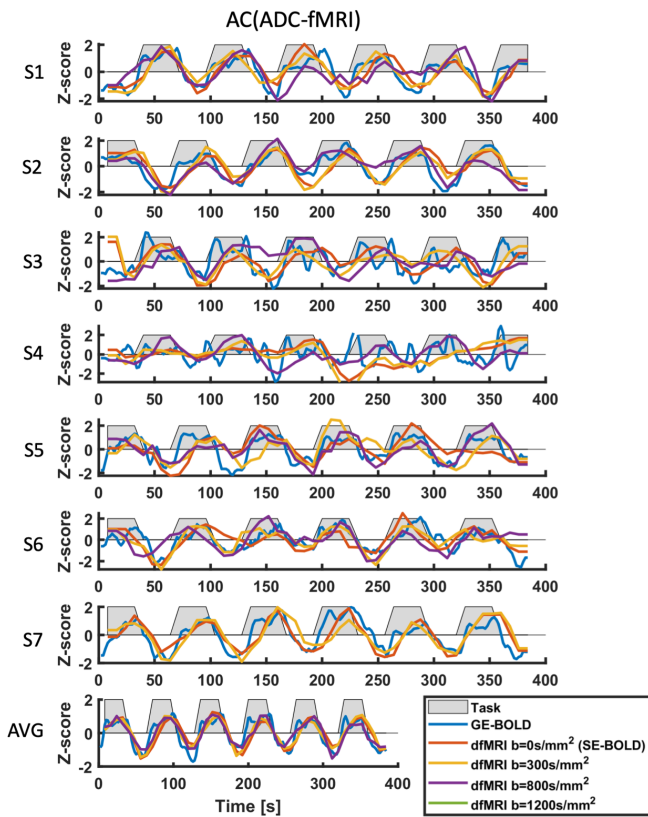
FIGURE 7 Sensitivity of GE-BOLD and ADC-fMRI in AC(ADC-fMRI). Z-scores of the time series of GE-BOLD and ADC-fMRI within the ADC-fMRI activation core. The individual ADC-fMRI signals showed signal changes up to 2 SDs in correspondence of task execution in line with GE-BOLD, irrespectively of the applied diffusion-weighting. The time series suggest that ADC-fMRI signals have higher delay to task execution than GE-BOLD. ADC, apparent diffusion coefficient; dfMRI, diffusion fMRI; fMRI, functional magnetic resonance imaging; GE-BOLD, gradient-echo blood oxygenation level dependent [Color figure can be viewed at wileyonlinelibrary.com]

sensitive to interactions with background gradients (Pampel, Jochimsen, & Möller, 2010). The interaction between the applied diffusion gradients and background contributions is effectively removed only when using bipolar or asymmetric gradient designs (Froeling, Strijkers, Nederveen, & Luijten, 2015), but has been predicted by Pampel et al. (2010) to be attenuated also by TRSE acquisitions (Reese, Heid, Weisskoff, & Wedeen, 2003). In particular, background gradients in the presence of deoxygenation have been shown to strongly decrease ADC values (Does, Zhong, & Gore, 1999), while simulations (Pampel et al., 2010) predict ADC values from monopolar gradients to be much less sensitive than TRSE to activation changes, configuring it as a potential confounder in our results. According to the study of Kohno et al. (2009), the effect of the cross terms would cause an overimposed diffusion weighting scaled between 1 and 10% the amplitude of the applied diffusion gradient, with dependence on the effective echo time, likely reducing the overall applied diffusion weighting. Applying the same reasoning to our results, dfMRI at b = 300 s/mm^2 could fall to a lower diffusion weighting, with increased sensitivity to vascular pools. However, in the case of dfMRI

at b = 800 or 1200 s/mm^2, this is less likely to happen. In practice, while the effect of cross terms could determine a bias in measures subsequently derived from dfMRI, for example, ADC-fMRI, it should not change the nature of the observed dfMRI signal changes in AC(dfMRI) and AC(ADC-fMRI) (Pampel et al., 2010). In support of this, we observed remarkable similarities between the above-mentioned studies employing both SE Stejskal–Tanner and TRSE sequences, and our findings of: (a) reduced activation extent and limited overlap of dfMRI as compared to GE-BOLD (Nicolas et al., 2017; Song et al., 2002) and (b) dfMRI signal increases and ADC$_{IVIM}$-fMRI decreases during activation (Le Bihan et al., 2006). The results presented here are therefore in general agreement with recent literature, suggesting potential advantages of dfMRI over GE-BOLD, especially in terms of spatial localization of the brain activated areas. However, it remains unclear whether the more focal activations detected with dfMRI (and ADC-fMRI) are closer to the real neuronal source of motor activation than conventional GE-BOLD fMRI activations, as recently suggested (Nunes et al., 2019).

Furthermore, we observed that both dfMRI and ADC-fMRI provide bilateral activations when comparing task and rest conditions, but that the overlap among the two is rather low, suggesting the detection of adjacent but not identical clusters. Establishing which of the two is closer to the neuronal activation will require further investigation, although our results suggest dfMRI as the most likely.

In conclusion, this study shows that the dfMRI signal is sensitive to task evoked activity, and that by employing appropriate diffusion weightings it is possible to investigate changes in different tissue domains. While dfMRI (and ADC-fMRI/f_{IVIM}-fMRI/ADC$_{IVIM}$-fMRI) is more challenging to perform and prone to artifacts than GE-BOLD, its selective sensitivity to different microstructural features has the potential to provide additional insights into brain activation mechanisms, to complement standard GE-BOLD.

CONFLICT OF INTEREST

None.

ORCID

Alberto De Luca https://orcid.org/0000-0002-2553-7299
Lara Schlaffke https://orcid.org/0000-0002-0716-3780
Jeroen C. W. Siero https://orcid.org/0000-0001-5079-2868

REFERENCES

Acheson, A., Wijtenburg, S. A., Rowland, L. M., Winkler, A., Mathias, C. W., Hong, L. E., ... Dougherty, D. M. (2017). Reproducibility of tract-based white matter microstructural measures using the ENIGMA-DTI protocol. *Brain and Behavior: A Cognitive Neuroscience Perspective*, 7, 1–10.

Akhlaghi, H., Corben, L., Georgiou-Karistianis, N., Bradshaw, J., Delatycki, M. B., Storey, E., & Egan, G. F. (2012). A functional MRI study of motor dysfunction in Friedreich's ataxia. *Brain Research*, 1471, 138–154. https://doi.org/10.1016/j.brainres.2012.06.035

Aso, T., Urayama, S., Poupon, C., Sawamoto, N., Fukuyama, H., & Le Bihan, D. (2009). An intrinsic diffusion response function for analyzing diffusion functional MRI time series. *NeuroImage*, 47, 1487–1495. http://www.ncbi.nlm.nih.gov/pubmed/19450693

Aso, T., Urayama, S. I., Fukuyama, H., & Le Bihan, D. (2013). Comparison of diffusion-weighted fMRI and BOLD fMRI responses in a verbal working memory task. *NeuroImage*, 67, 25–32. https://doi.org/10.1016/j.neuroimage.2012.11.005

Chandarana, H., Lee, V. S., Hecht, E., Taouli, B., & Sigmund, E. E. (2011). Comparison of biexponential and monoexponential model of diffusion weighted imaging in evaluation of renal lesions: Preliminary experience. *Investigative Radiology*, 46, 285–291. http://www.embase.com/search/results?subaction=viewrecord&from=export&id=L51165120%5Cnhttps://doi.org/10.1097/RLI.0b013e3181ffc485%5Cnhttp://elvis.ubvu.vu.nl:9003/vulink?sid=EMBASE&issn=00209996&id=doi:10.1097/RLI.0b013e3181ffc485&atitle=Comparison+of+b

Cho, G. Y., Moy, L., Zhang, J. L., Baete, S., Lattanzi, R., Moccaldi, M., ... Sigmund, E. E. (2015). Comparison of fitting methods and b-value sampling strategies for intravoxel incoherent motion in breast cancer. *Magnetic Resonance in Medicine*, 74, 1077–1085. http://www.ncbi.nlm.nih.gov/pubmed/25302780

Dale, A. M., Fischl, B., & Sereno, M. I. (1999). Cortical surface-based analysis. I. Segmentation and surface reconstruction. *NeuroImage*, 9, 179–194. http://www.ncbi.nlm.nih.gov/pubmed/9931268

Darquié, A., Poline, J. B., Poupon, C., Saint-Jalmes, H., & Le Bihan, D. (2001). Transient decrease in water diffusion observed in human occipital cortex during visual stimulation. *Proceedings of the National Academy of Sciences of the United States of America*, 98, 9391–9395. http://www.ncbi.nlm.nih.gov/pubmed/11459931

De Luca, A., Leemans, A., Bertoldo, A., Arrigoni, F., & Froeling, M. (2018). A robust deconvolution method to disentangle multiple water pools in diffusion MRI. *NMR in Biomedicine*, 31, e3965. https://doi.org/10.1002/nbm.3965

Does, M. D., Zhong, J., & Gore, J. C. (1999). In vivo measurement of ADC change due to intravascular susceptibility variation. *Magnetic Resonance in Medicine*, 41, 236–240.

Federau, C., Maeder, P., O'Brien, K., Browaeys, P., Meuli, R., & Hagmann, P. (2012). Quantitative measurement of brain perfusion with intravoxel incoherent motion MR imaging. *Radiology*, 265, 874–881. http://pubs.rsna.org/doi/10.1148/radiol.12120584

Federau, C., O'Brien, K., Birbaumer, A., Meuli, R., Hagmann, P., & Maeder, P. (2015). Functional mapping of the human visual cortex with intravoxel incoherent motion MRI. *PLoS One*, 10, e0117706. http://www.ncbi.nlm.nih.gov/pubmed/25647423

Fields, R. D. (2011). Signaling by neuronal swelling. *Science Signaling*, 4, tr1. http://www.ncbi.nlm.nih.gov/pubmed/21224445

Finkenstaedt, T., Klarhoefer, M., Eberhardt, C., Becker, A. S., Andreisek, G., Boss, A., & Rossi, C. (2017). The IVIM signal in the healthy cerebral gray matter: A play of spherical and non-spherical components. *NeuroImage*, 152, 340–347. https://doi.org/10.1016/j.neuroimage.2017.03.004

Froeling, M., Strijkers, G. J., Nederveen, A. J., & Luijten, P. R. (2015). Whole heart DTI using asymmetric bipolar diffusion gradients. *Journal of Cardiovascular Magnetic Resonance*, 17, P15. http://jcmr-online.biomedcentral.com/articles/10.1186/1532-429X-17-S1-P15

Glielmi, C. B., Xu, Q., Craddock, R. C., & Hu, X. (2010). Simultaneous acquisition of gradient echo/spin echo BOLD and perfusion with a separate labeling coil. *Magnetic Resonance in Medicine*, 64, 1827–1831. http://www.ncbi.nlm.nih.gov/pubmed/20648682

Glover, G. H. (1999). Deconvolution of impulse response in event-related BOLD fMRI. *NeuroImage*, 9, 416–429. http://www.ncbi.nlm.nih.gov/pubmed/10191170

Goense, J. B. M., & Logothetis, N. K. (2006). Laminar specificity in monkey V1 using high-resolution SE-fMRI. *Magnetic Resonance Imaging*, 24, 381–392.

Grech-Sollars, M., Hales, P. W., Miyazaki, K., Raschke, F., Rodriguez, D., Wilson, M., ... Clark, C. A. (2015). Multi-centre reproducibility of diffusion MRI parameters for clinical sequences in the brain. *NMR in Biomedicine*, 28, 468–485.

Gudbjartsson, H., & Patz, S. (1995). The Rician distribution of noisy MRI data. *Magnetic Resonance in Medicine*, 34, 910–914. http://www.ncbi.nlm.nih.gov/pubmed/8598820

Iima, M., & Le Bihan, D. (2016). Clinical intravoxel incoherent motion and diffusion MR imaging: Past, present, and future. *Radiology*, 278, 13–32. http://www.ncbi.nlm.nih.gov/pubmed/26690990

Jenkinson, M., Bannister, P., Brady, M., & Smith, S. (2002). Improved optimization for the robust and accurate linear registration and motion correction of brain images. *NeuroImage*, 17, 825–841. http://www.ncbi.nlm.nih.gov/pubmed/12377157

Jenkinson, M., Beckmann, C. F., Behrens, T. E. J., Woolrich, M. W., & Smith, S. M. (2012). FSL. *NeuroImage*, 62, 782–790. http://www.ncbi.nlm.nih.gov/pubmed/21979382

Keil, V. C., Mädler, B., Gielen, G. H., Pintea, B., Hiththetiya, K., Gaspranova, A. R., ... Hadizadeh, D. R. (2017). Intravoxel incoherent motion MRI in the brain: Impact of the fitting model on perfusion fraction and lesion differentiability. *Journal of Magnetic Resonance Imaging*, 46, 1187–1199. http://www.ncbi.nlm.nih.gov/pubmed/28152250

Klein, S., Staring, M., Murphy, K., Viergever, M. A., & Pluim, J. P. W. (2010). Elastix: A toolbox for intensity-based medical image registration. *IEEE Transactions on Medical Imaging*, 29, 196–205. http://www.ncbi.nlm.nih.gov/pubmed/19923044

Klein, S., Staring, M., & Pluim, J. P. W. (2007). Evaluation of optimization methods for nonrigid medical image registration using mutual information and B-splines. *IEEE Transactions on Image Processing*, 16, 2879–2890. http://ieeexplore.ieee.org/lpdocs/epic03/wrapper.htm?arnumber=4374125

Koh, D. M., Collins, D. J., & Orton, M. R. (2011). Intravoxel incoherent motion in body diffusion-weighted MRI: Reality and challenges. *American Journal of Roentgenology*, 196, 1351–1361.

Kohno, S., Sawamoto, N., Urayama, S., Aso, T., Aso, K., Seiyama, A., ... Le Bihan, D. (2009). Water-diffusion slowdown in the human visual cortex on visual stimulation precedes vascular responses. *Journal of Cerebral Blood Flow and Metabolism*, 29, 1197–1207. http://journals.sagepub.com/doi/10.1038/jcbfm.2009.45

Le Bihan, D., Breton, E., Lallemand, D., Aubin, M. L., Vignaud, J., & Laval-Jeantet, M. (1988). Separation of diffusion and perfusion in intravoxel incoherent motion MR imaging. *Radiology*, 168, 497–505. http://pubs.rsna.org/doi/10.1148/radiology.168.2.3393671

Le Bihan, D., Urayama, S., Aso, T., Hanakawa, T., & Fukuyama, H. (2006). Direct and fast detection of neuronal activation in the human brain with diffusion MRI. *Proceedings of the National Academy of Sciences of the United States of America*, 103, 8263–8268. http://www.pnas.org/content/103/21/8263?tab=ds

Leemans, A., Jeurissen, B., Sijbers, J., & Jones, D. K. (2009): *ExploreDTI: a graphical toolbox for processing, analyzing, and visualizing diffusion MR data*. In 17th Annual Meeting of the International Society for Magnetic Resonance in Medicine, Honolulu, HI p 3537.

Miller, K. L., Bulte, D. P., Devlin, H., Robson, M. D., Wise, R. G., Woolrich, M. W., ... Behrens, T. E. J. (2007). Evidence for a vascular contribution to diffusion FMRI at high b value. *Proceedings of the*

National Academy of Sciences of the United States of America, *104*, 20967–20972. http://www.pnas.org/content/104/52/20967.short

Nicolas, R., Gros-Dagnac, H., Aubry, F., & Celsis, P. (2017). Comparison of BOLD, diffusion-weighted fMRI and ADC-fMRI for stimulation of the primary visual system with a block paradigm. *Magnetic Resonance Imaging*, *39*, 123–131.

Norris, D. G., Zysset, S., Mildner, T., & Wiggins, C. J. (2002). An investigation of the value of spin-echo-based fMRI using a Stroop color-word matching task and EPI at 3 T. *NeuroImage*, *15*, 719–726. http://www.ncbi.nlm.nih.gov/pubmed/11848715

Nunes, D., Ianus, A., & Shemesh, N. (2019). Layer-specific connectivity revealed by diffusion-weighted functional MRI in the rat thalamocortical pathway. *NeuroImage*, *184*, 646–657. https://doi.org/10.1016/j.neuroimage.2018.09.050

Pampel, A., Jochimsen, T. H., & Möller, H. E. (2010). BOLD background gradient contributions in diffusion-weighted fMRI—Comparison of spin-echo and twice-refocused spin-echo sequences. *NMR in Biomedicine*, *23*, 610–618.

Pasternak, O., Sochen, N., Gur, Y., Intrator, N., & Assaf, Y. (2009). Free water elimination and mapping from diffusion MRI. *Magnetic Resonance in Medicine*, *62*, 717–730. http://www.ncbi.nlm.nih.gov/pubmed/19623619

Pierpaoli, C., & Jones, D. K. (2004): *Removing CSF Contamination in Brain DT-MRIs by Using a Two-Compartment Tensor Model C*. In International Society for Magnetic Resonance in Medicine, Kyoto, Japan.

Provenzale, J. M., Engelter, S. T., Petrella, J. R., Smith, J. S., & MacFall, J. R. (1999). Use of MR exponential diffusion-weighted images to eradicate T2 "shine-through" effect. *AJR. American Journal of Roentgenology*, *172*, 537–539. http://www.ncbi.nlm.nih.gov/pubmed/9930819

Reese, T. G., Heid, O., Weisskoff, R. M., & Wedeen, V. J. (2003). Reduction of eddy-current-induced distortion in diffusion MRI using a twice-refocused spin echo. *Magnetic Resonance in Medicine*, *49*, 177–182. http://www.ncbi.nlm.nih.gov/pubmed/12509835

Rudrapatna, U. S., van der Toorn, A., van Meer, M. P. A., & Dijkhuizen, R. M. (2012). Impact of hemodynamic effects on diffusion-weighted fMRI signals. *NeuroImage*, *61*, 106–114. http://www.ncbi.nlm.nih.gov/pubmed/22406501

Rydhög, A. S., Szczepankiewicz, F., Wirestam, R., Ahlgren, A., Westin, C.-F., Knutsson, L., & Pasternak, O. (2017). Separating blood and water: Perfusion and free water elimination from diffusion MRI in the human brain. *NeuroImage*, *156*, 423–434. http://www.sciencedirect.com/science/article/pii/S1053811917303154

Setsompop, K., Gagoski, B. A., Polimeni, J. R., Witzel, T., Wedeen, V. J., & Wald, L. L. (2012). Blipped-controlled aliasing in parallel imaging for simultaneous multislice echo planar imaging with reduced g-factor penalty. *Magnetic Resonance in Medicine*, *67*, 1210–1224.

Sigmund, E. E., Vivier, P.-H., Sui, D., Lamparello, N. A., Tantillo, K., Mikheev, A., … Chandarana, H. (2012). Intravoxel incoherent motion and diffusion-tensor imaging in renal tissue under hydration and furosemide flow challenges. *Radiology*, *263*, 758–769.

Smith, S. M. (2002). Fast robust automated brain extraction. *Human Brain Mapping*, *17*, 143–155. http://www.ncbi.nlm.nih.gov/pubmed/12391568

Song, A. W., Woldorff, M. G., Gangstead, S., Mangun, G. R., & McCarthy, G. (2002). Enhanced spatial localization of neuronal activation using simultaneous apparent-diffusion-coefficient and blood-oxygenation functional magnetic resonance imaging. *NeuroImage*, *17*, 742–750. http://www.ncbi.nlm.nih.gov/pubmed/12377149

Song, A. W., Wong, E. C., Tan, S. G., & Hyde, J. S. (1996). Diffusion weighted fMRI at 1.5 T. *Magnetic Resonance in Medicine*, *35*, 155–158. http://www.ncbi.nlm.nih.gov/pubmed/8622577

Tsurugizawa, T., Ciobanu, L., & Le Bihan, D. (2013). Water diffusion in brain cortex closely tracks underlying neuronal activity. *Proceedings of the National Academy of Sciences of the United States of America*, *110*, 11636–11641.

van Baalen, S., Leemans, A., Dik, P., Lilien, M. R., Ten Haken, B., & Froeling, M. (2017). Intravoxel incoherent motion modeling in the kidneys: Comparison of mono-, bi-, and triexponential fit. *Journal of Magnetic Resonance Imaging*, *46*, 228–239. http://www.ncbi.nlm.nih.gov/pubmed/27787931

Williams, R. J., McMahon, K. L., Hocking, J., & Reutens, D. C. (2014). Comparison of block and event-related experimental designs in diffusion-weighted functional MRI. *Journal of Magnetic Resonance Imaging*, *40*, 367–375.

Winston, G. P. (2012). The physical and biological basis of quantitative parameters derived from diffusion MRI. *Quantitative Imaging in Medicine and Surgery*, *2*, 254–265. http://www.pubmedcentral.nih.gov/articlerender.fcgi?artid=3533595&tool=pmcentrez&rendertype=abstract

Yacoub, E., Uludağ, K., Uğurbil, K., & Harel, N. (2008). Decreases in ADC observed in tissue areas during activation in the cat visual cortex at 9.4 T using high diffusion sensitization. *Magnetic Resonance Imaging*, *26*, 889–896.

Zhang, Y., Brady, M., & Smith, S. (2001). Segmentation of brain MR images through a hidden Markov random field model and the expectation-maximization algorithm. *IEEE Transactions on Medical Imaging*, *20*, 45–57. http://www.ncbi.nlm.nih.gov/pubmed/11293691

SUPPORTING INFORMATION

Additional supporting information may be found online in the Supporting Information section at the end of this article.